ACS APPLIED MATERIALS & INTERFACES

www.acsami.org

Research Article

Side-Chain-Based Cross-Linking of Amorphous Iono-Electronic Conductive Polymers for Thermo-Chemical Stability in Electrochemical Devices

Heejung Roh,[#] Simone Bagatella,[#] Shuwen Yue, Aditi Seshadri, Changhwan Oh, Camille E. Cunin, Marco Cavallaro, Marinella Levi, Heather J. Kulik, and Aristide Gumyusenge*

Cite This: https://doi.org/10.1021/acsami.6c05214

Read Online

ACCESS | Metrics & More | Article Recommendations | Supporting Information

ABSTRACT: Robust electrochemical modulation and environmental stability remain difficult to co-optimize with performance in organic semiconductors. Using a poly (propylenedioxythiophene) (ProDOT)-based polymer as an amorphous model conductor, we show that carbene-enabled and selective formation of covalent linkages between side-chains enhances thermo-chemical robustness while optimizing device performance. While pristine films of ProDOT degrade at ∼130 °C and dissolve in common solvents, cross-linked films retain physicochemical properties, redox activity, and stability (>2000 cycles) under such conditions. Upon cross-linking, mixed conduction follows a nonmonotonic, volcano-like profile, peaking at ∼6 wt % diazirine used as the cross-linker, where transconductance (g_m) is enhanced by ∼35-fold and remains stable under external stress when integrated in organic electrochemical transistors (OECTs). Implementation of cross-linked films in electrochemical random access memory (ECRAM) devices demonstrates a performance profile that uniquely combines analog metrics that are comparable to state-of-the-art—large dynamic range (>30×), robust write/erase endurance (>120,000 pulses), high linearity, and training accuracy (>90%)—with thermo-chemical robustness under harsh conditions, which has been a longstanding bottleneck for the applicability of organic semiconductors in scalable manufacturing. This side-chain-based cross-linking is a versatile strategy to impart robustness and enable facile postsynthetic tuning of mixed conduction, especially for amorphous semiconducting polymers, unlocking their practical use in next-generation iono-electronic and computing hardware.

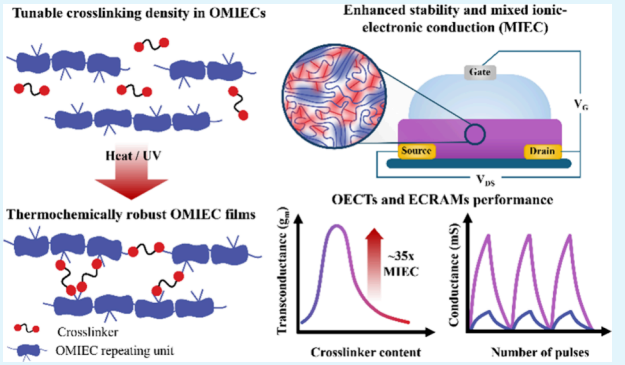

KEYWORDS: *cross-linking, organic semiconductors, organic electrochemical transistors, blends, composites*

INTRODUCTION

Polymer-based organic semiconductors offer unique advantages, such as solution processability, lightweight properties, mechanical flexibility, low cost, and large-area fabrication.[1−5] More recently, organic mixed ionic-electronic conductors (OMIECs) have driven a resurgence in organic electronics, especially adaptive on-body computing. In particular, when employed as channel materials in organic electrochemical transistors and electrochemical random access memory (OECTs and ECRAMs), these materials have enabled emerging applications spanning from bioelectronics to low-power neuromorphic in-memory computing.[6−13] Efforts to enhance performance in these devices have been directed toward two key aspects: developing new semiconducting channel materials and/or engineering device architectures. Environmental resistance, particularly to temperature and chemicals, which represent the most common and restrictive factors, is highly desirable for (i) device fabrication, ensuring compatibility with nanofabrication processes, such as thermal deposition, annealing, and photolithographic processes like etching; and (ii) operational stability in OECT and ECRAM devices under practically relevant, nonideal conditions. Theoretically, higher temperatures should enhance conductivity in conjugated polymers (i.e., semiconductors), since charge carriers rely on a thermally activated hopping mechanism for transport.[14−17] In practice, however, this benefit is counteracted by disrupted molecular packing in polymer thin films at elevated temperatures,[18,19] thereby limiting the range of viable applications.

To address performance degradation, strategies such as wide-bandgap material engineering, thermal-resistant pack-

Received: March 13, 2026
Revised: June 9, 2026
Accepted: June 10, 2026

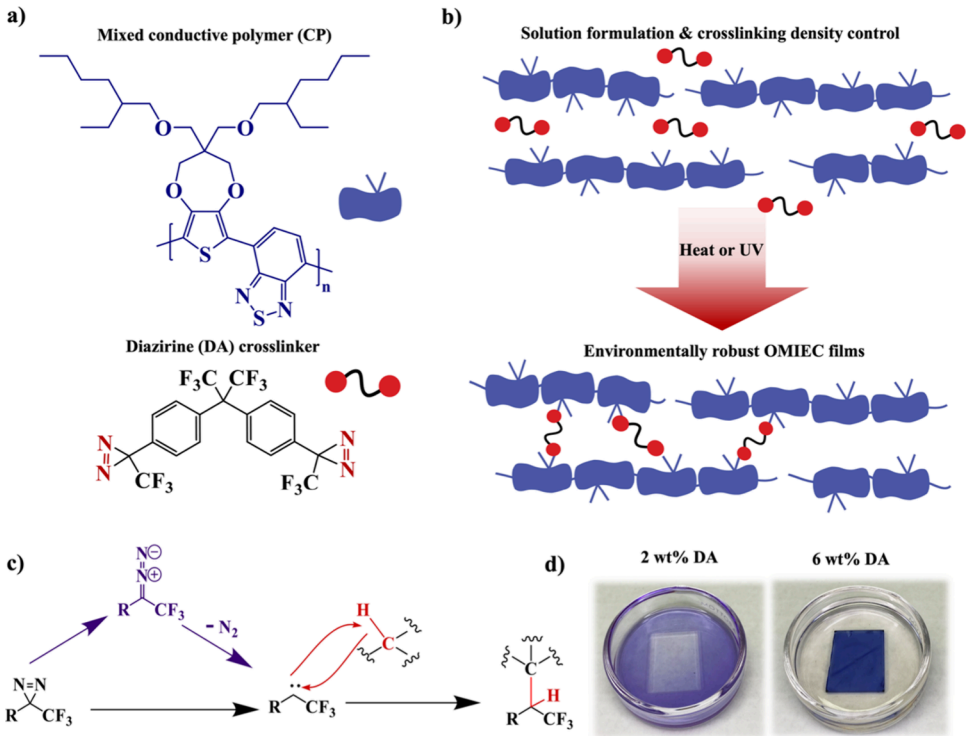

Figure 1. Bis-diazirine-based cross-linking strategy to impart thermo-chemical robustness in amorphous polymer films. (a) Chemical structures of a nearly amorphous polymer (ProDOT:BTD) and diazirine cross-linker (termed CP and DA, respectively, throughout the text). (b, c) Cross-linking of polymer through carbene formation followed by C−H insertion. (d) Photographs of films, without and with cross-linking, after 5 min in chloroform.

aging, isolation, and cooling systems have often been adopted.[20] In polymer electronics, blending semiconducting polymers with insulating hosts has been one of the most successful strategies to improve electronic performance, processability, and mechanical and environmental stability in electronic devices.[5,21−24] For instance, blending with high T_g insulating matrices was reported to achieve temperature-insensitive charge transport behavior up to 220 °C in thin-film transistors.[5,25,26] Incorporation of small-molecule cross-linkers is another general strategy for tuning the properties of conducting polymers (CPs), primarily enhancing mechanical strength and corrosion resistance while preserving the homogeneity of the host material.[27−30]

In this context, cross-linking of OMIECs has also been recently explored, particularly using diazirine (DA), demonstrating its potential for improving device stability.[29,31−33] However, these studies primarily utilized cross-linking for channel patterning purposes, aiming for higher resolution, minimizing leakage and crosstalk, and device scaling.[31,34] While cross-linking has been used to impart mechanical resilience and flexibility in CPs, a systematic understanding of how cross-linking degree and backbone crystallinity, together, dictate electrochemical function under thermochemical stress remains lacking. Herein, we introduce bis-diazirine as a cross-linker to impart thermo-chemical robustness and enable tuning of mixed conduction through controlled cross-linking density. Using electrochromic polymers, we systematically examined its impact on (i) thermochemical stability, (ii) physicochemical properties, (iii) solid-state packing and morphology, (iv) polymer-ion interactions and redox activity, and (v) mixed ionic-electronic performance across films with varied cross-linking density.

RESULTS AND DISCUSSION

As shown in previous works by our group, propylenedioxythiophene benzothiadiazole (ProDOT:BTD, hereafter termed as CP unless otherwise noted) copolymer is a promising channel material for OECTs and synaptic devices (Figure 1a).[8,35] We thus selected this CP as a model system due to its high charge storage capacity, low-energy redox switching, and redox cycling stability.[36−41] However, the nearly amorphous nature that facilitates ion uptake and transport also makes ProDOT:BTD highly susceptible to external stressors such as high temperatures, solvent exposure, as well as prolonged operation. Its performance deteriorates under these conditions because, intrinsically, the polymer lacks strong interchain and interdomain interactions to offset entropic penalties. Note that this limitation is not unique to ProDOT:BTD; many polymeric OMIECs rely on flexible aliphatic or ionophilic side-chains and backbones to promote ionic insertion, which often results in amorphous structures inherently vulnerable to environmental factors.

To address this challenge, we selected bis-diazirine (DA, Figure 1a) as the cross-linker owing to the following merits:[42−48] (i) it enables a broadly applicable cross-linking strategy across organic polymers with C−H bond formation, (ii) it requires no initiators or additives, (iii) it is target-specific toward side-chains and hence has minimal effects on the conjugated backbone (Figure 1b), and (iv) it preserves the inherent stacking and morphology, as side-chains typically reside in amorphous regions of the film. Unlike previously reported cross-linkers for OMIECs,[49−51] DA cross-links through alkyl side-chains (thus mostly targeting the amorphous regions of the film bulk) and enables nanoscale morphology retention without perturbing the crystalline domains needed

https://doi.org/10.1021/acsami.6c05214
ACS Appl. Mater. Interfaces XXXX, XXX, XXX−XXX

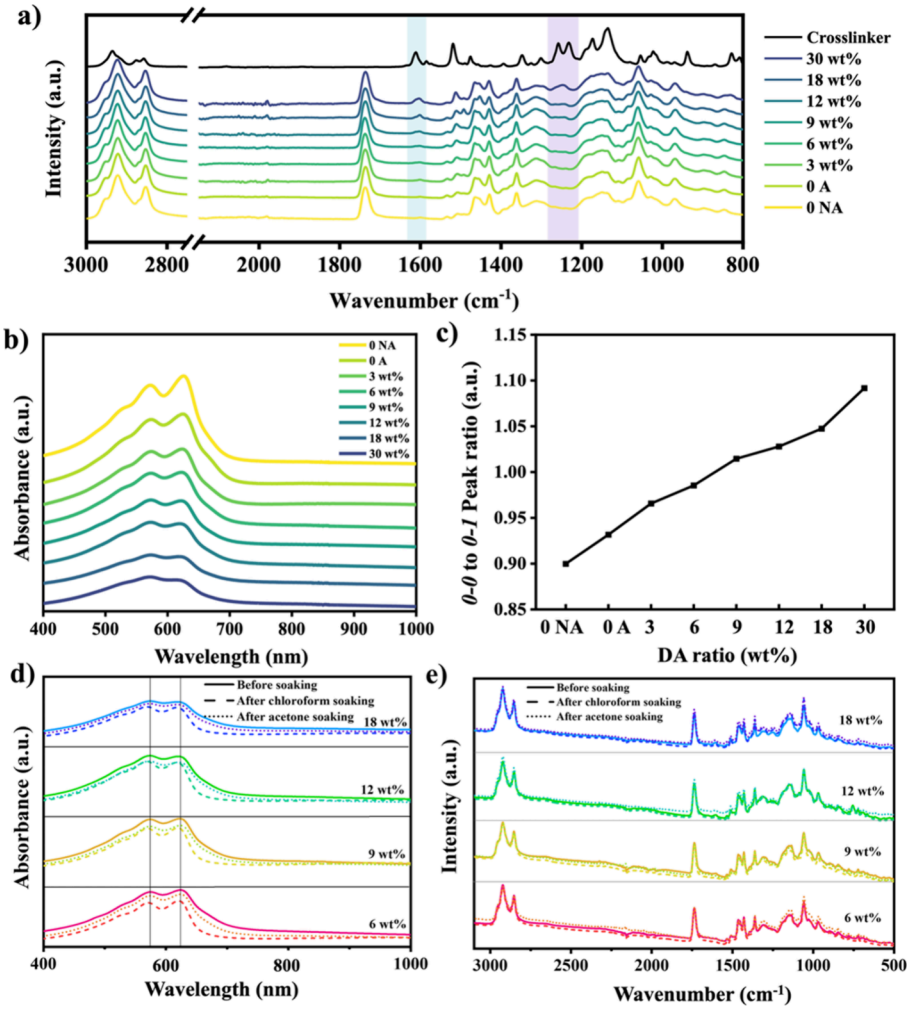

Figure 2. (a) FTIR spectra of films of the pristine cross-linker and cross-linked CP with varied DA ratios (i.e., cross-linking density). (b) UV−vis absorption spectra of pristine and cross-linked CPs with the DA ratio ranging from 0 to 30 wt %. (c) Relative changes in absorption intensity associated with interbackbone (0−0) and intrabackbone (0−1) charge-transfer transitions (0−0/0−1). (d, e) Solid-state physicochemical stability against thermochemical stress. *Ex situ* UV−vis absorption (d) and FTIR (e) spectra after 2 h of exposure to commonly used solvents.

for charge transport. To ensure broader applicability and reliability, we selected a commercially available bis-diazirine derivative. With this small molecule, the cross-linking occurs through a well-documented mechanism illustrated in Figure 1b,c as previously reported.[42−48] Briefly, upon gentle heating or UV light exposure, diazirine undergoes a bond cleavage to release nitrogen gas, leaving behind a reactive carbene intermediate. With its high electrophilicity, carbene then readily reacts with the C−H bonds, forming covalent bonds, either with carbon atoms in adjacent polymer chains or within the same chain, creating a moderately cross-linked network.

As shown in Figures 1d and S1 (Supporting Information), cross-linked films withstand extended soaking in harsh solvents that readily dissolve pristine CP films and cross-linkers, such as chloroform and acetone. Under the same conditions, pristine CP (as-cast and annealed, 0 NA and 0 A, respectively) and lightly cross-linked (3 wt %) samples dissolved completely. In contrast, higher-density cross-linked films with ≥6 wt % DA remained intact, showing no dissolution even after vigorous shaking, sonication, and over a week (7 consecutive days) of immersion, with the solvents staying clear (Figure S2 and Video 1, Supporting Information). This demonstrates that cross-linking converts a two-phase physical mixture into a chemically bonded homogeneous network and that a minimum DA loading (∼6 wt %) is required for the film to be stable.

From the FTIR spectra, the absence of any absorption near ∼2100 cm^{-1} confirms that diazirine activation proceeds cleanly to carbene without accumulation of diazo byproducts, particularly the linear diazo intermediate (Figure 2a).[42−44,47,52] Instead, the pristine cross-linker spectrum exhibits a distinct absorption at ∼1590 cm^{-1}, attributed to the −N═N− stretching of the diazirine ring, which vanishes upon cross-linking and complete consumption of diazirine units during carbene-mediated C−H insertion. Concomitantly, with increasing cross-linking density, the peak at 1610 cm^{-1}, characteristic of the aromatic C═C stretch in the pristine cross-linker,[53] intensifies, reflecting both the higher proportion of linker incorporated into the matrix and the retention of its aryl structure. Another characteristic peak that increases in intensity with cross-linking appears around 1240 cm^{-1}, corresponding to the stretching vibration of the C−F group present in the cross-linker.[54] Importantly, the major vibrational peaks associated with the polymer backbone remained unchanged (e.g., C−H stretching ∼2918 cm^{-1}), confirming that the cross-linking occurs through the side-chains while

https://doi.org/10.1021/acsami.6c05214
ACS Appl. Mater. Interfaces XXXX, XXX, XXX−XXX

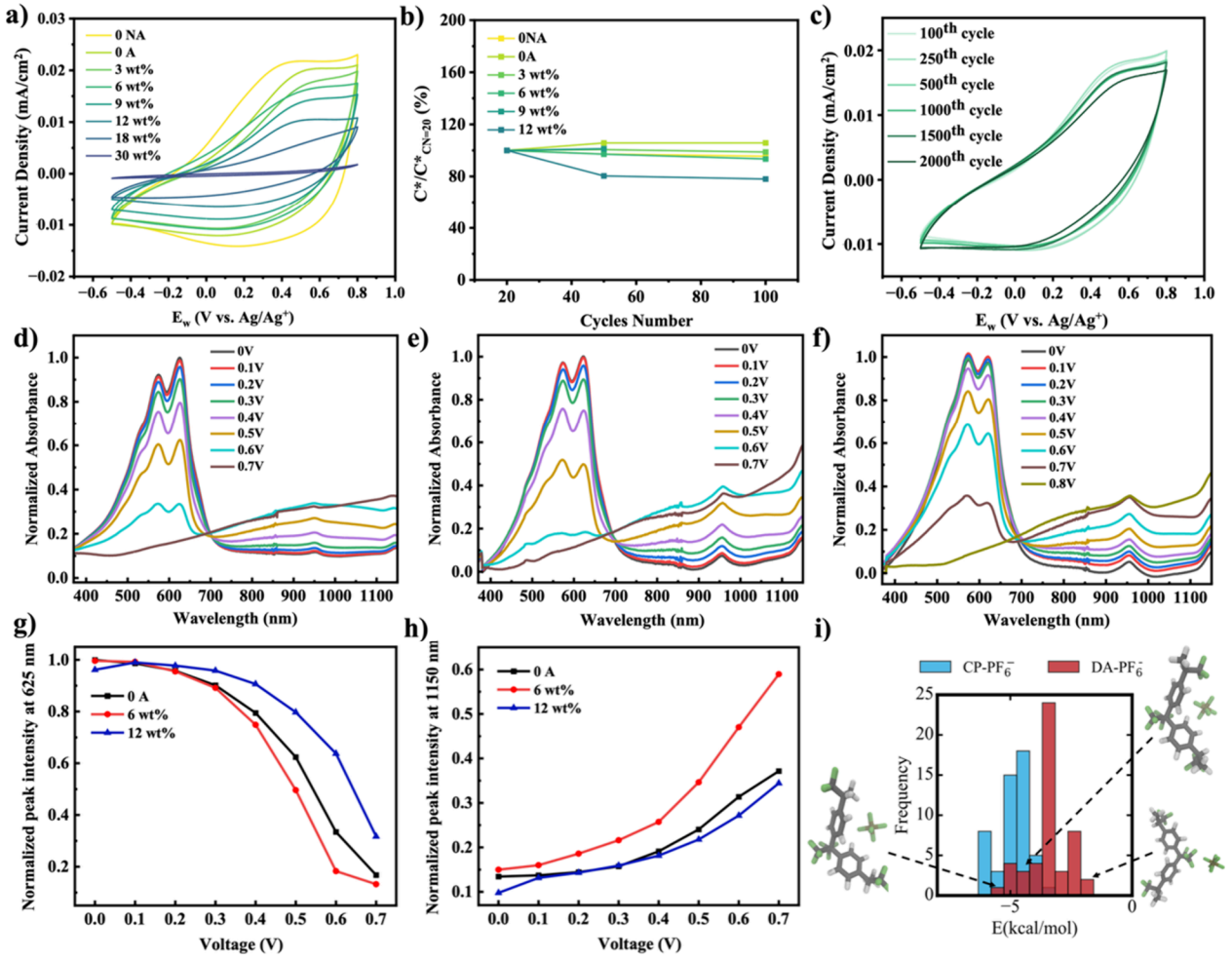

Figure 3. Impact of cross-linking on electrochemical properties (activity, capacitance, and redox stability). (a, b) Cyclic voltammograms of control and cross-linked films with varying DA ratios in 0.1 M $LiPF_6$. (c) Cyclic stability of volumetric capacitance (C^*) cross-linked samples (6 wt %) in 0.1 M $LiPF_6$. (d–f) Spectro-electrochemistry spectra in 0.1 M $LiPF_6$ under 0–0.8 V of (d) 0 A, (e) 6 wt %, and (f) 12 wt % DA. (g, h) Extracted absorbance at the wavelengths of 625 and 1150 nm, respectively. (i) Distributions of binding energies of the anion (PF_6^-) to CP and DA units, with molecular diagrams of representative configurations of the anion and DA associated with a given binding energy (corresponding molecular diagrams with configurations of the anion and CP are shown in ref 35). C atoms are in gray, O atoms are in red, H atoms are in white, and F atoms are in green. The binding energy is defined as $E_{Binding} = E_{DA\text{-}anion} - E_{anion} - E_{DA}$.

preserving backbone chemistry across all DA concentrations. Thermogravimetric analysis of these films revealed progressively higher degradation temperatures with increasing cross-linker loading, consistent with the formation of a covalent network rather than simple physical mixing (Figure S3, Supporting Information). That is, the lack of weight loss proportional to cross-linker content (relative to pristine CP) indicates complete reaction of the cross-linkers, since any unreacted small molecules would have volatilized and contributed to measurable mass loss.

We used Raman spectroscopy to track C=C (conjugation-related) peaks and assess electronic structure changes as previously demonstrated in CPs.[55,56] Notably, three broad peaks at 1423, 1456, and 1517 cm^{-1} corresponding to $C_\alpha{=}C_\beta$ (−O) symmetric stretching in the middle of the chains, CH_2/CH_3 bending, and $C_\alpha{=}C_\beta$ asymmetric stretching at the end of the chains remain unchanged even at a cross-linker ratio of 18 wt % (Figure S4, Supporting Information).[55−57] This suggests that the conjugated backbone remains relatively preserved, as no significant bond breakage or rearrangement was detected in those specific vibrational regions. Backbone integrity was also evident from UV–vis absorption spectra (Figure 2b,c), which showed an intrachain vibronic transition 0–1 peak near 573 nm and a strong interchain vibronic transition 0–0 peak near 625 nm, characteristic of ProDOT:BTD.[58,59] The cross-linked films showed no peak shift, indicating that the cross-linking reaction between aliphatic side-chains does not perturb the main chain. This intrachain charge-transfer feature of the CP is retained, even after 4 months of storage at ambient (Figure S5, Supporting Information). Similarly, the amorphous nature of CP was confirmed to persist upon cross-linking using X-ray diffraction (Figure S6, Supporting Information).

Notably, with increasing DA content, the vibronic 0–0/0–1 peak ratio increased progressively, from 0.93 at 0 wt % (0 A) to 0.97, 0.98, 1.01, 1.03, 1.05, and 1.09 at 3, 6, 9, 12, 18, and 30 wt %, respectively (Figures 2b,c and S7, Supporting Information). This suggested that interchain interactions and chain aggregation are likely the most affected by cross-linking, as DA molecules occupy the amorphous domains of the films. Indirectly, this hypothesis was corroborated using a relatively more crystalline polymer (namely, poly(3-hexylthiophene-2,5-diyl), P3HT), where DA molecules are barely allowed into the

https://doi.org/10.1021/acsami.6c05214
ACS Appl. Mater. Interfaces XXXX, XXX, XXX−XXX

crystalline bulk; minimal change in the 0−0/0−1 peak ratio could be observed (Figure S7, Supporting Information).

The effect of DA-based cross-linking on chemical and thermal tolerance was confirmed by comparing the solid-state properties (e.g., UV−vis and FTIR) of the polymer films before and after exposure to harsh environments. As shown in Figure 2d,e, no significant changes in the spectra could be detected upon different chemical stressors, indicative of enhanced chemoresistance enabled by bonding neighboring chains together. Note that the pristine CP films are fully dissolved upon immersion in the solvents (Figures S1 and S2, Supporting Information). In pristine CP (0 NA) samples, the 0−0/0−1 absorbance ratio decreased progressively from 1.12 to 1.08, 1.03, and 1.01 upon exposure to 70, 120, and 170 °C for 2 h, respectively, accompanied by a slight shift in the 0−0 transition peak (Figure S8, Supporting Information). In contrast, cross-linked films exhibited stable absorbance ratios after thermal treatment, maintaining values of 1.01 (130 °C, 2 h), 1.01 (150 °C, 2 h), 1.02 (170 °C, 2 h), and 1.02 (130 °C, 5 h) (Figure S9, Supporting Information). Importantly, this stability was independent of DA loading, with even 9 wt % films retaining the initial pristine absorbance value. This indicates that the more pronounced spectral changes in pristine samples arise primarily from polymer chain deaggregation and rearrangement rather than dilution by cross-linkers. Preserved peak positions (0−0 and 0−1 transitions) and relative intensities in UV−vis (Figure 2d) and FTIR spectra (Figure 2e) in *ex situ* measurements with samples exposed to thermal stress and solvent soaking further corroborated the imparted robustness.

We then employed electrochemical characterizations to evaluate how cross-linking density influences film properties. The addition of DA results in a decrease in volumetric capacitance (C^*) (Figure 3a). Under identical cycling conditions, C^* decreased with increasing DA content (from 0 A to 30 wt %) from a value of 146 to 7 F cm^{-3} in aqueous electrolyte (Figures S10 and S11, Supporting Information), consistent with dilution of the electroactive polymer by electrochemically inactive cross-linkers. A similar decrease (from 319 to 105 F cm^{-3} for 0 A and 30 wt %, respectively) was observed in the nonaqueous (EMIM:TFSI) electrolyte (Figure S12, Supporting Information). Nonetheless, the oxidation peak (~0.43 V vs Ag/Ag$^+$) present in the pristine control (0 A) remained clearly visible and nearly the same (~0.5 V ± 0.03 vs Ag/Ag$^+$) in cross-linked films (6 and 12 wt %) in both aqueous and nonaqueous electrolytes, confirming preservation of the intrinsic redox properties of the pristine CP. Reaching a cross-linking amount of 18 wt %, the peak collapsed, and at 30 wt %, the film barely showed any capacitance, as shown in Figures 3a and S10 (Supporting Information). The cross-linked films showed excellent redox-switching stability, maintaining C^* over more than 2000 (de)doping cycles at a fast scan rate of 20 mV/s (Figure 3b,c). Notably, after 2000 cycles, the sample with 6 wt % DA showed a 16% increase in C^* (compared to the value at 100 cycles), while the sample with 12 wt % DA showed a decrease of 26% in C^* (Figure S11, Supporting Information). Similar behavior was observed in nonaqueous EMIM:TFSI (Figure S12, Supporting Information). All samples retained more than 90% of their initial capacitance even after 2000 cycles, whereas pristine references degraded to 54 and 55% after 500 cycles, respectively, highlighting remarkable stability even in the presence of DA. For 6 wt % samples, the nonaqueous EMIM:TFSI electrolyte gave higher C^* (249 F cm^{-3}) than the aqueous $LiPF_6$ (146 F cm^{-3}).

Figures 3d−f and S13 (Supporting Information) show the recorded absorption spectra from films with varied cross-linking densities (0 A, 3, 6 and 12 wt %) in 0.1 M $LiPF_6$ aqueous electrolyte. As the working potential increases, the intensity of the π-π transition ~650 nm decreases and eventually vanishes at the critical voltage, while the absorption at $\lambda_{polaron}$ ~ 1150 nm intensifies, evidencing polaron formation and increased carrier density. This transition corresponds to electrochemical switching from the colored (neutral) to the bleached (doped) state. The control (0 NA) films exhibited bleaching of $\lambda_{max(\pi-\pi)}$ at ~ +0.2 V (vs Ag/Ag$^+$), as reported in our previous work,[35] whereas the annealed counterpart (0 A) required substantially higher bleaching voltages (~ +0.7 V), indicating a loss in electrochemical accessibility upon thermal annealing of pristine CP films. In contrast, cross-linked samples retained high electrochemical activity. Systematic variation of cross-linker density revealed a peak at 6 wt %, where the peak at 650 nm bleaches with ~ +0.4 V, well below the ~ +0.7 and ~ +0.6 V required for 3 and 0 wt % films, respectively (Figure 3e,f). This switching behavior reflects balanced ion uptake and electronic conjugation: cross-linkers stabilize amorphous regions by restricting uncontrolled morphological changes upon ion incorporation, preserve interconnected CP backbones for rapid percolation, and leave sufficient free volume for ion transport. Over-cross-linking (above 12 wt %), however, hindered redox activity, shifting the $\lambda_{max(\pi-\pi^*)}$ bleaching to ~ +0.7 V and slowing doping/dedoping, indicating restricted ion penetration and disrupted pathways. Concomitant polaron growth in the NIR and apparent visible bleaching confirmed efficient charge-carrier generation, which is the fastest at 6 wt % DA.

Collectively, we hypothesize that this behavior originates from retained electrical conjugation among CP chains, enabled by the suppression of uncontrolled swelling under electrochemical charging, while retaining sufficient free volume for ion injection/transport.[58,60] At this optimum, electrical responses from counterion doping propagate rapidly through the bulk, sustaining redox activity during fast potential sweeps as apparent reversible redox bleaching and coloration. Notably, binding energy calculations through DFT show that the cross-linker itself does not repel electrolyte ions: binding energies between bis-diazirine and the studied ions in electrolytes are comparable to those with CP building blocks (Figures 3g and S14 and S15, Supporting Information),[35,61,62] indicating that diminished activity at higher loadings arises not from chemical incompatibility but from physical restriction of ion incorporation and transport under high cross-linking density. Thus, this neighboring effect is countered by the inability of ions to adequately incorporate into the densely cross-linked network, providing the main rationale for why cross-linking density must remain moderate: excessive cross-linking prevents sufficient swelling, so even with well-bound chains, ion insertion becomes limited. However, these DFT calculations evaluate static binding energies and, therefore, probe thermodynamic compatibility alone. The comparable ion-cross-linker and ion-backbone binding energies indicate that the cross-linker does not energetically reject or trap electrolyte ions relative to the host polymer, whereas dynamic transport limitations, such as diffusion barriers, segmental mobility, and free-volume distributions, are not captured by this approach.

https://doi.org/10.1021/acsami.6c05214
ACS Appl. Mater. Interfaces XXXX, XXX, XXX−XXX

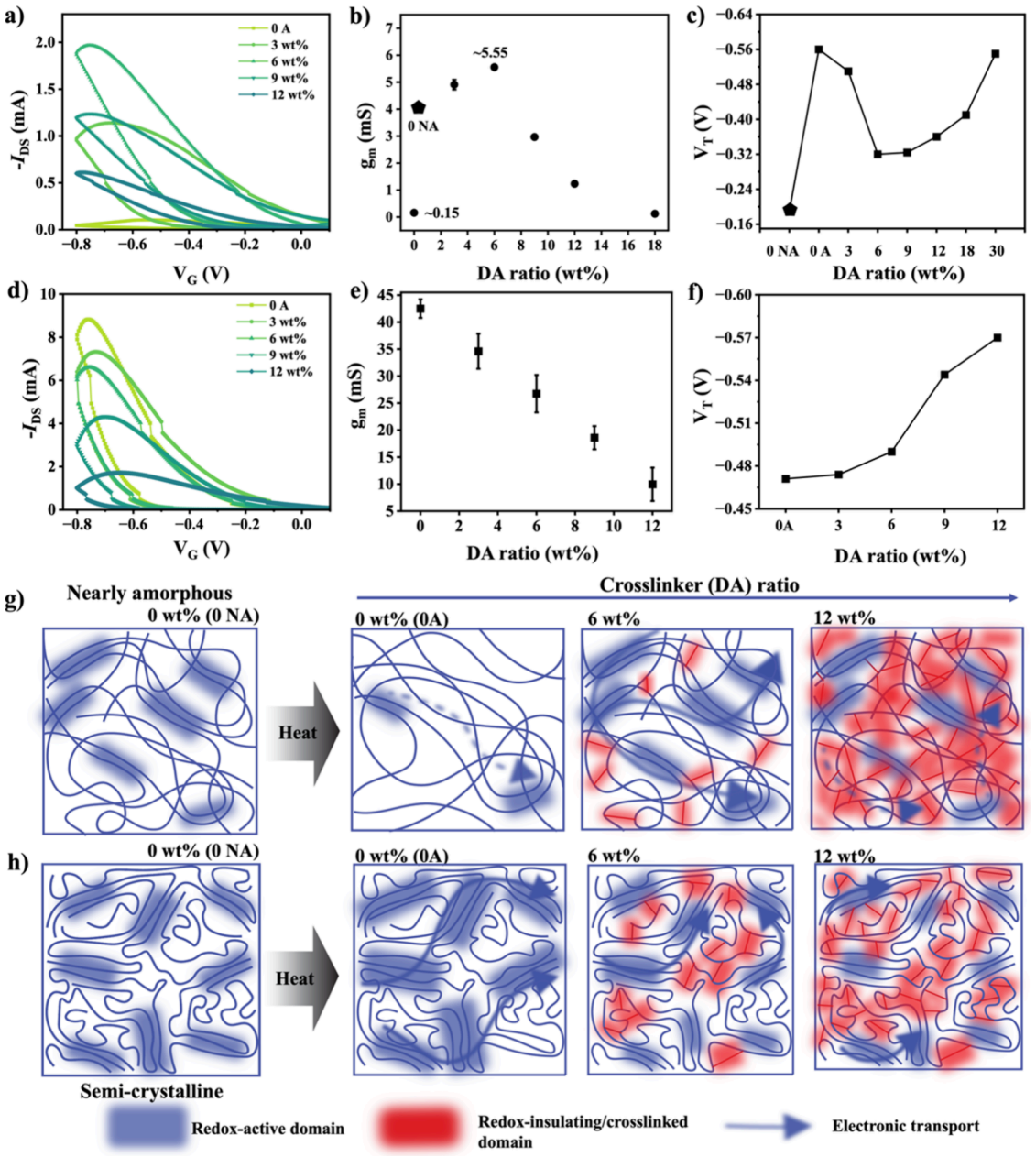

Figure 4. Influence of cross-linking density and host matrix order on mixed ionic-electronic conduction performance in OECT devices in 0.1 M aqueous electrolyte. Transfer curves (a, d), extracted transconductance (b, e), and threshold voltage (c, f) with varied DA ratios of nearly amorphous CP (a–c) and semicrystalline P3HT (d–f), respectively. Proposed generic microscopic framework to explain the volcanic profile in mixed conductivity with increasing cross-linking density in (g) nearly amorphous CP and (h) semicrystalline CP, and how the impact of cross-linking density on mixed conductivity depends upon host polymer crystallinity. The crystallinity of the host CP governs the structural integrity of the pristine film upon exposure to external stimuli (e.g., thermal, chemical stress).

To assess the iono-electronic coupling and amplification performance in cross-linked films, OECT devices were measured using aqueous and nonaqueous electrolytes. The measured transfer curves and extracted parameters, including transconductance (g_m) and threshold voltage (V_T), are shown, respectively, for nearly amorphous ProDOT:BTD (Figure 4a–c, respectively) and the semicrystalline polymer P3HT (Figure 4d–f, respectively). Additional details on device fabrication and characterization can be found in the Supporting Information (Figures S16–S20, Supporting Information). Notably, for the nearly amorphous polymer, device performance exhibited a nonmonotonic, volcano-like dependence on DA content, reaching a maximum at 6 wt % (5.55 ± 0.09 mS), a ~35-fold increase in g_m compared to the 0 A films (0.16 ± 0.02 mS), before decreasing to 1.23 ± 0.09 and 0.12 ± 0.01 mS at 12 and 18 wt %, respectively (Figure 4b). The cycling stability of the best-performing 6 wt % DA OECT was further characterized over 100 consecutive sweepsand showed to retain its initial peak current with negligible decay and showing reproducible transfer-curve profiles throughout 70 cycles (Figures S22 and S23, Supporting Information). The same volcanic profile of I_{peak} and g_m, peaking at 6 wt %, was observed in the nonaqueous electrolyte (EMIM:TFSI, Figure S21, Supporting Information). This is consistent with the electrochemical activity discussed above for peaking at 6 wt %, where significantly lower voltage was required to reach equivalent

https://doi.org/10.1021/acsami.6c05214
ACS Appl. Mater. Interfaces XXXX, XXX, XXX–XXX

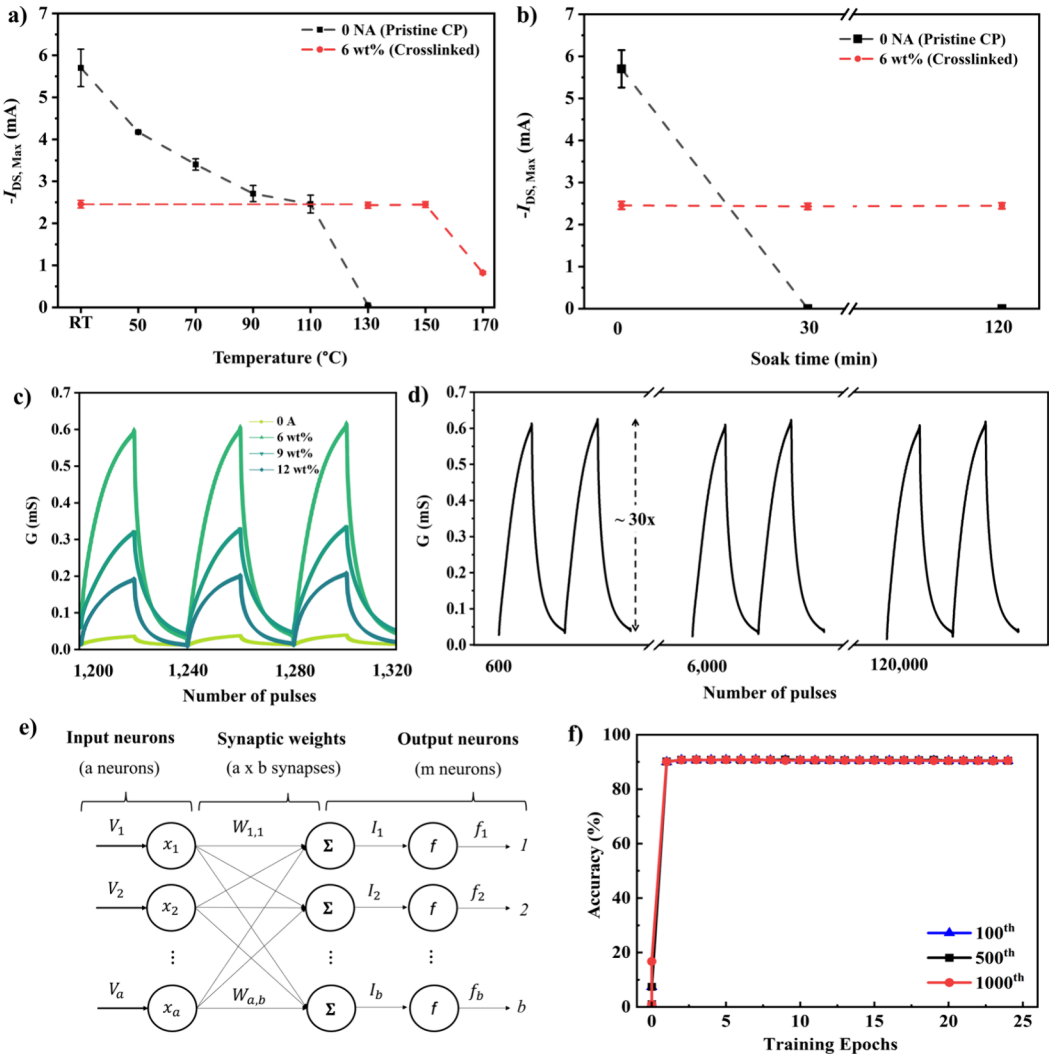

Figure 5. Thermochemical robustness of devices based on cross-linked CPs. Average $-I_{DS,Max}$ from transfer curves upon (a) 2 h of heating at gradually increasing temperatures and (b) prolonged soaking of the device in acetone. (c) Reversible conductance changes in response to a series of train pulses with different polarities (i.e., write/erase) from ECRAM devices with varied cross-linking densities. The detailed pulsing profile is shown in Figure S29a, Supporting Information. (d) Endurance performance of 6 wt % over extended pulsing numbers. (e) Working mechanism of the single-layer logistic regression model used to recognize the standard data set of MNIST (Figure S29b, Supporting Information). (f) Accuracy of image recognition tests with respect to training epochs to further evaluate the accuracy retention capability.

doping levels, and the fastest polaron formation was observed through *in situ* spectro-electrochemistry. In contrast, over-cross-linking (>6 wt % DA) led to delayed responses and reduced activity, reflecting restricted ion penetration and disrupted transport pathways. The counterintuitive enhancement in mixed ionic-electronic conduction, despite a lower redox-active fraction, and its peak at intermediate cross-linking densities (~6 wt % DA) arise from the multifaceted role of cross-linking in conjugated polymer matrices.

First, cross-linking imparts thermochemical robustness under harsh conditions by maintaining structural integrity against solvent-induced dissolution and thermal disordering of the polymer chains. Second, this stabilization preserves electrical percolation by protecting backbone conjugation and $\pi-\pi$ stacking interactions that are critical for efficient electronic transport. Third, cross-linking does not energetically repel ions or hinder ion transport, as binding energies between cross-linkers and mobile ions are comparable to those with the polymer backbone while maintaining sufficient free volume, allowing ion insertion, migration, and storage. However, at excessive cross-linking, the disruption of crystalline domains and electrical percolation indicates the optimal balance between ionic accessibility and electronic percolation is required. This volcanic mechanism is further corroborated by electrochemical impedance spectroscopy (EIS). Equivalent-circuit fitting of the Nyquist plots (Figure S24 and Table S1, Supporting Information) yields a nonmonotonic dependence of the bulk electronic charge-transfer resistance, R_{ct} (6 wt % < 0 A < 0 NA < 12 wt %), with the 6 wt % film exhibiting the lowest R_{ct} of the series. While cross-linker incorporation inherently dilutes the redox-active fraction, this optimal loading (6 wt %) suppresses excessive morphological disorder while preserving interchain ordering and electronic connectivity. Conversely, at excessive loadings (≥18 wt %), the active fraction drops below the percolation threshold, physically disconnecting the conducting domains and drastically increasing R_{ct} (Figure S24 and Table S1, Supporting Information). Building on this, we propose a generic conceptual framework for microscopic configurational tuning of the host polymer matrix via cross-linking, offering a strategy

https://doi.org/10.1021/acsami.6c05214
ACS Appl. Mater. Interfaces XXXX, XXX, XXX−XXX

to modulate mixed conduction through structural control (Figure 4g,h). A critical assumption underlying this behavior, consistent with prior studies on the effect of small-molecule cross-linking density within polymers on stretchability,[63] is that cross-linking occurs predominantly in the amorphous regions of the polymer matrix. Accordingly, the physical effects of cross-linking, such as network stabilization, electrical percolation (e.g., redox-active content ratio, crystalline domain connectivity), and ion transport (e.g., free volume, energetic interaction), depend strongly on both the degree of cross-linking and the availability of amorphous domains. Thereby, the position of this peak in mixed ionic-electronic conduction along the cross-linking density depends on the initial crystallinity of the host matrix: amorphous-rich systems exhibit a maximum at intermediate cross-linking densities, where stabilization of the disordered domains provides the greatest benefit.

In contrast, highly crystalline or semicrystalline polymers effectively peakwithout the cross-linker, since additional cross-linking primarily disrupts ordered domains without offering compensatory stabilization. The decrease observed at excessive cross-linking occurs beyond the peak when the saturation of amorphous regions drives cross-linker intrusion into ordered domains. This disrupts $\pi-\pi$ stacking, dilutes the redox-active content, and severely compromises electronic percolation. This mechanism is supported by semicrystalline P3HT, which shows a monotonic decline in performance due to limited amorphous volume: even low cross-linking levels disrupt ordered packing, effectively shifting the optimum (seen as a volcanic peak) toward essentially as low as 0 wt %. This trend is consistent with prior reports showing that the threshold for cross-linking-induced disruption of crystalline domains depends on the crystallinity of the host matrix (Figure 4g,h). We anticipate that side-chain length, flexibility, polarity, and branching will further modulate the position of this volcano: longer or more flexible side-chains provide greater amorphous volume and shift the optimum to higher DA loadings, whereas shorter or more rigid side-chains compress it to lower DA wt %, consistent with the collapse to ∼0 wt % in the more crystalline P3HT system (Figure 4d−f). This trend further highlights the role of polymer architecture in defining the optimal cross-linking window.

We further tested the proposed stabilization mechanism on the performance of OECT and ECRAM devices operated upon exposure to various external stressors including temperature, solvent exposure, and extended cycling. Pristine CP devices gradually degraded in performance when subjected to thermal stress (Figure 5a). Compared to room temperature conditions, I_{peak} in the transfer and output current decreased to 66.6% at 50 °C, 55.2% at 70 °C, 43.3% at 90 °C, 42.5% at 110 °C, and 0.05% at 130 °C (Figures S25−S28, Supporting Information). In contrast, cross-linked devices (6 wt %) maintained a stable performance with preserved I_{peak} values as high as 2.50 ± 0.09 mA before exposure, which is preserved within 5%, even after heating for extended periods of time (130 °C for 5 h or 150 °C for 2 h, Figures 5a and S28, Supporting Information). Note that the current showed a dramatic drop to 0.82 ± 0.03 mA when the temperature was raised to as high as 170 °C (for 2 h). The sharper drop above 150 °C may reflect crossing an effective thermal threshold of the cross-linked network: below it (130−150 °C), the network likely remains in a glassy/elastic regime where the microscopic morphology would be fully recovered on cooling. However, above this range, transient segmental motion likely perturbs interchain pathways and leads to irreversible morphological changes on cooling, while the polymer chemistry itself remains intact (Figures 2e and S9). Similarly, *ex situ* OECT device characteristics upon solvent (acetone) exposure revealed that the non-cross-linked samples were completely damaged, whereas the cross-linked devices retained their I_{peak} values: 2.45 ± 0.09 mA before exposure and 2.43 ± 0.07 and 2.44 ± 0.07 mA after 30 min and 2 h of full immersion in acetone, respectively (Figure 5b).

In ECRAM devices, samples with varied DA ratios exhibited reversible conductance (G) updates in response to alternating write/erase pulses. As shown in Figures 5c and S30 (Supporting Information), consistent with the volcano-like trend observed in mixed ionic-electronic conduction (i.e., I_{peak} and g_m), the 6 wt % sample (Figure 5d), which showed the highest balanced mixed ionic-electronic conduction quantified by peak transfer current and transconductance, exhibited the largest dynamic range (defined as the conductance difference between high and low states) as high as 0.56 mS. The cross-linked films demonstrate excellent endurance in repeated write/erase, an essential criterion for practical artificial synapses capable of performing complex tasks such as image recognition, despite the smaller dynamic range as the DA ratio increases with the order of 6 wt % DA > 12 wt % DA > 0 A (Figures S30 and S31, Supporting Information). This memristive property enables ionic memory, where conductance states encode prior voltage histories (and corresponding ionic insertion) through prolonged ionic redistribution, supporting analog weight updates in ECRAMs. This phenomenon is further corroborated by spectro-electrochemistry, which tracks absorption spectra across consecutive stepwise voltage sweeps. The low absorbance ratio of $\lambda_{\pi-\pi^*}$ and $\lambda_{polaron}$ was retained even during the second cycle, evidencing the persistence of generated charge carriers (polarons) and thus a possibility of memory effect (Figure S32a,b, Supporting Information). Furthermore, the stepwise reversibility of conductance modulation was observed, where applying an opposite bias (−0.4 V) restored the initial state, marked by the clear reappearance of the prominent $\pi-\pi^*$ peak and attenuation of the polaron peak (Figure S32c,d, Supporting Information). The accuracy of training ECRAMs based on 6 wt % CP films on a benchmark handwritten digit recognition task exceeds 90% after 5 training epochs. Furthermore, such accuracy levels were also retained after over 1000 cycles (>120,000 pulses), demonstrating linear weight modulation, efficient learning, and superior endurance (Figure 5d−f and Table 2, Supporting Information). This dynamic range and linearity could also be maintained in cross-linked films, after exposure to harsh thermal and chemical conditions (Figures S33−S34 and Table 3, Supporting Information). These findings demonstrate that the cross-linking approach largely preserves the physical properties and performance in CPs, enabling practical use of devices.

CONCLUSIONS

In this work, we propose a generic conceptual framework for microscopic configurational tuning of the host polymer matrix via cross-linking, offering a strategy to modulate mixed conduction through structural control. We leverage diazirine-based carbene chemistry to covalently cross-link the otherwise van der Waals-bound CP chains via selective C−H insertion in aliphatic side-chains. As such, we impart thermochemical

https://doi.org/10.1021/acsami.6c05214
ACS Appl. Mater. Interfaces XXXX, XXX, XXX−XXX

robustness and enable facile, postsynthetic tuning of mixed conduction while preserving the intrinsic solid-state physicochemical properties of the host CP. Cross-linking suppresses chain slippage and uncontrolled entropic disorder in amorphous regions, maintaining network integrity and imparting robustness against configurational disruption even under thermochemical stress. The observed nonmonotonic (i.e., volcanic) trend of mixed conduction with cross-linking density reflects a trade-off between structural reinforcement and disruption of electronic percolation. The optimal balance is achieved at 6 wt %, which stabilizes the network (unlike 3 wt % films, which still dissolve in solvent) while delivering the highest redox activity and OECT conductivity. These properties remain stable over extended cycling (up to 2000 cycles) and elevated temperatures and harsh solvent exposure. However, beyond 6 wt % cross-linker density, saturation of the amorphous regions drives intrusion into ordered domains, disrupting $\pi-\pi$ stacking, diluting the redox-active content, and compromising electronic percolation. This effect is particularly pronounced in semicrystalline P3HT, where even low cross-linking levels perturb the chain packing due to the limited amorphous volume, shifting the optimum effectively toward 0 wt %. Complementary computational analysis further supports that the loss of electronic percolation, rather than ionic mobility, is the primary factor limiting performance at higher cross-linking densities. As a proof-of-concept, the optimal 6 wt % composition was integrated into an ECRAM device, which exhibited state-of-the-art endurance and training accuracy and retained performance even after *ex situ* thermochemical stress. Together, these findings establish a broadly applicable design framework for tailoring CP-cross-linker chemistry, addressing key practical limitations across a wide library ofconjugated polymers, and enabling robust, customizable mixed conductors for emerging electrochemical applications.

EXPERIMENTAL SECTION

Materials and Sample Preparation

CP ($M_n \sim 16$ kDa, $Đ = 1.5$) was synthesized following reported procedures[64] and supplied by the Mei Research Group at Purdue University. Poly(3-hexylthiophene-2,5-diyl) (P3HT, $M_W \sim 35.3$ kDa, $Đ = 1.3$), electrolyte salts (e.g., $LiPF_6$, EMIM:TFSI, LiTFSI, LiCl, NaCl), and ITO-coated glass slides were purchased from Sigma-Aldrich. DA (BondLynx) was obtained from XLYNX Materials, Inc. and used as received. Si/SiO_2 wafers were purchased from University Wafer. Control and cross-linked CP films for characterizations were obtained via the following steps: (i) ProDOT:BTD and DA were codissolved in chloroform at 15 mg mL^{-1} at the desired DA wt %; (ii) the blend was spin-coated at 800 rpm for 40 s onto the substrate; (iii) the film was transferred to a vacuum oven preheated to 130 °C and annealed for 2 h (unless otherwise indicated), and diazirine activation proceeds via thermolysis (>110 °C); and (iv) the films (Figure S1) were obtained after cooling under vacuum to room temperature before further characterization. For *ex situ* thermochemical tests, samples were heated under specified temperature−time conditions in vacuum or immersed in chemical solvents and then stored and characterized under ambient conditions.

Electrochemical Characterization

CV measurements were carried out using a conventional 3-electrode electrochemical cell setup. ITO substrates (one-side conductive) were sequentially cleaned by sonication in deionized water (60 °C), acetone, and isopropanol, followed by drying with nitrogen. Polymer films coated onto ITO served as a working electrode and a spiral Pt wire was used as a counter electrode versus a Ag/Ag^+ reference electrode. The volumetric capacitance (C^*) for each polymer was obtained using the CV curves according to the following equation:

$$C^* = \frac{\int iV\,dV}{2 \cdot t \cdot (V_{\text{Positive\_end}} - V_{\text{Negative\_end}}) \cdot k} \quad (1)$$

where i is the current density, V is the voltage vs Ag/Ag^+, t is the film thickness, k is the scan speed, and $\int iV\,dV$ is the area under the CV scan calculated using the integration function in OriginLab software. $V_{\text{Positive\_end}}$ and $V_{\text{Negative\_end}}$ are the maximum and minimum voltages of the CV scan range, respectively. In situ spectro-electrochemical absorption responses were then collected using a PerkinElmer Lambda 1050 UV−vis−NIR spectrophotometer in combination with an SP-300 potentiostat (Biologic), using a cuvette (purchased from Sterna Cell) to incorporate the 3-electrode setup.

Electrical Conductivity Measurements

Electrical conductivity of the composite films was evaluated using a Keithley 4200 analyzer in a four-point probe configuration and calculated using the following equation:

$$\sigma = \frac{1}{R}\frac{l}{A} \quad (2)$$

where σ is the electronic conductivity, R is the resistance measured, l is the film thickness obtained by the Dektak profilometer, and A is the area.

Calculational Details: Ion-Cross-Linker (or Polymer) Binding Energies via Implicit Solvation DFT

All calculations were carried out using Orca 5.0.0 with the def2-TZVP basis set, the B3LYP global hybrid functional, and the empirical D4 dispersion correction with Becke−Johnson damping. The calculations were performed in implicit solvent using the conductor-like polarizable continuum model (CPCM) with the dielectric constant of bulk water. To assess preferential ion binding in the cross-linked matrix, we compared DFT binding energies for five ions (Na^+, Li^+, Cl^-, PF_6^-, $TFSI^-$) interacting with a representative cross-linker unit against previously reported ion-CP polymer values.[34] The binding energy was evaluated from an ensemble of configurations generated by sampling ion placements around a methyl-capped cross-linker followed by constrained relaxations; binding energies were computed as $E_{\text{bind}} = E_{\text{cross-linker+ion}} - E_{\text{ion}} - E_{\text{cross-linker}}$.

Device Fabrication

Devices (channel dimensions of $L = 5$ μm and $W = 400$ μm) were fabricated in the cleanroom environment (Class 100) at MIT, and source and drain electrodes were defined using photolithography with AZnLOF2020 photoresist and a mask-less aligner (Heidelberg MLA 150). A 10 nm layer of Ti (Kurt J. Lesker) followed by a 100 nm layer of Au (Kurt J. Lesker) was deposited using an e-beam evaporator (Temescal FC2000). Subsequently, a first layer of parylene-C was deposited using a Specialty Coating Systems PDS 2010, employing Silane A 174 (procured from Sigma-Aldrich) as an adhesion promoter. A sacrificial layer of 2% MICRO-90 soap (VWR) in DI water was spin-coated onto the wafer before depositing a second layer of parylene-C. The channel and electrode pads were then defined using the same mask-less aligner with AZ10XT photoresist and a reactive ion etching process (SAMCO 230iP). Channels were formed by dynamically spin-coating 15 mg mL^{-1} solutions of pristine CP and blends with DA onto the devices at 800 rpm for 40 s. Following a peel-off step, the devices underwent a residual solvent evaporation step before characterization. A PDMS slab was cut to form a well and used to contain the electrolytes. The transfer, output, pulsing, and transfer stability characteristics of the OECT devices were measured using a Keithley 4200A, with a Ag/AgCl pellet serving as the gate.

Endurance Measurements

Electrical characterizations and pulsed measurements (synaptic device performance) were carried out using a probe station, Keithley 4200 analyzer, in an ambient condition (room temperature and open air). The pulsed measurements were programmed using an ultrafast pulse

https://doi.org/10.1021/acsami.6c05214
ACS Appl. Mater. Interfaces XXXX, XXX, XXX−XXX

measure unit coupled with a remote pre-amplified module. OECT performances were obtained by applying a gate voltage (V_G) from 0 to −0.8 V, and the source-drain voltage (V_{DS}) was set to −0.8 V. A constant voltage bias was applied to either source or drain, while the other one was grounded to read the synaptic current flowing between the source and drain terminals. To program the pulses, we applied voltage pulses from the gate (V_G = 0 to −0.8 V) with both time interval (T_d) and pulse width (Δt) set between 10 and 40 ms. For endurance tests, a series of identical potentiation pulses was applied with varying counts (e.g., 10−300 times) followed by the same number of depression pulses.

Learning Accuracy: Modeling Synaptic Conductance Using MNIST Digit Recognition

A single-layer perceptron was trained using our synaptic devices and trained on the standard MNIST data set. The network consisted of 785 input neurons (28 × 28 pixels plus bias) and 10 output neurons with a softmax layer. During training, synaptic weights were updated by comparing softmax predictions with ground-truth labels using cross-entropy loss and the Adaptive Moment Estimation (Adam) optimizer. We employed a hardware-based backpropagation (HDBP) scheme in which each weight is represented by a differential synapse pair ($W = G^+ - G^-$). For each update, the sign of ΔW determined whether G^+ or G^- underwent potentiation or depression.

$$\Delta G = G_{n+1} - G_n = \begin{cases} \alpha e^{-\beta G_n - G_{min}/G_{max} - G_{min}}, & \text{if state} = \text{potentiation}(\Delta W > 0) \\ -\alpha e^{-\beta G_{max} - G_n/G_{max} - G_{min}}, & \text{if state} = \text{depression}(\Delta W < 0) \end{cases} \quad (3)$$

G_n and G_{n+1} represent the synapse conductance before and after each training update. The step size α and nonlinearity β define the conductance update functions, which are fitted to the experimentally measured synaptic behaviors. All simulations were performed using Python with SciPy v.1.12.0 and PyTorch packages.

■ ASSOCIATED CONTENT

Supporting Information

The Supporting Information is available free of charge at https://pubs.acs.org/doi/10.1021/acsami.6c05214.

0, 3, 6, 9, and 12 wt % DA in chloroform (MOV)

Additional experimental details, supplemental figures, and tables (PDF)

■ AUTHOR INFORMATION

Corresponding Author

Aristide Gumyusenge − *Department of Materials Science & Engineering, Massachusetts Institute of Technology, Cambridge, Massachusetts 02139, United States;* orcid.org/0000-0003-4995-5222; Email: aristide@mit.edu

Authors

Heejung Roh − *Department of Materials Science & Engineering, Massachusetts Institute of Technology, Cambridge, Massachusetts 02139, United States*

Simone Bagatella − *Department of Materials Science & Engineering, Massachusetts Institute of Technology, Cambridge, Massachusetts 02139, United States; Department of Chemistry, Materials and Chemical Engineering "Giulio Natta", Politecnico di Milano, 20133 Milano, Italy;* orcid.org/0000-0001-5347-7345

Shuwen Yue − *Robert F. Smith School of Chemical and Biomolecular Engineering, Cornell University, Ithaca, New York 14853, United States;* orcid.org/0000-0002-1259-4649

Aditi Seshadri − *Robert F. Smith School of Chemical and Biomolecular Engineering, Cornell University, Ithaca, New York 14853, United States*

Changhwan Oh − *Department of Materials Science & Engineering and Department of Chemical Engineering, Massachusetts Institute of Technology, Cambridge, Massachusetts 02139, United States;* orcid.org/0000-0003-2120-6676

Camille E. Cunin − *Department of Materials Science & Engineering, Massachusetts Institute of Technology, Cambridge, Massachusetts 02139, United States*

Marco Cavallaro − *Department of Chemistry, Materials and Chemical Engineering "Giulio Natta", Politecnico di Milano, 20133 Milano, Italy*

Marinella Levi − *Department of Chemistry, Materials and Chemical Engineering "Giulio Natta", Politecnico di Milano, 20133 Milano, Italy*

Heather J. Kulik − *Department of Chemical Engineering and Department of Chemistry, Massachusetts Institute of Technology, Cambridge, Massachusetts 02139, United States;* orcid.org/0000-0001-9342-0191

Complete contact information is available at: https://pubs.acs.org/10.1021/acsami.6c05214

Author Contributions

#H.R. and S.B. contributed equally to this work.

Notes

The authors declare no competing financial interest.

■ ACKNOWLEDGMENTS

H.R. acknowledges the Surpina and Panos Eurnekian Nanotechnology Fund Fellowship from MIT. H.R. and A.G. acknowledge support in the form of a seed grant from the Abdul Latif Jameel Water & Food Systems (JWAFS) Lab at MIT. A.G. also thanks the research group of Prof. Jianguo Mei for supplying the polymer materials. C.E.C. received support from the K. Lisa Yang Brain Body Center at MIT and the MIT HEALS Graduate Fellowship. S.B. acknowledges financial support from the Progetto Roberto Rocca Doctoral Fellowship. C.O. and H.J.K. acknowledge a grant from Murata, LLC. Part of this work made use of the shared experimental facilities including the MIT.nano, the Materials Research Laboratory (MRL), and the Department of Chemistry Instrumentation Facility (DCIF) at MIT.

■ REFERENCES

(1) Mei, J.; Diao, Y.; Appleton, A. L.; Fang, L.; Bao, Z. Integrated Materials Design of Organic Semiconductors for Field-Effect Transistors. *J. Am. Chem. Soc.* **2013**, *135* (18), 6724−6746.

(2) Crone, B.; Dodabalapur, A.; Lin, Y.-Y.; Filas, R. W.; Bao, Z.; LaDuca, A.; Sarpeshkar, R.; Katz, H. E.; Li, W. Large-Scale Complementary Integrated Circuits Based on Organic Transistors. *Nature* **2000**, *403* (6769), 521−523.

(3) Root, E. S.; Savagatrup, S.; Printz, D. A.; Rodriquez, D.; Lipomi, J. D. Mechanical Properties of Organic Semiconductors for

Stretchable, Highly Flexible, and Mechanically Robust Electronics. *Chem. Rev.* **2017**, *117* (9), 6467−6499.
(4) Li, H.; Shi, W.; Song, J.; Jang, H.-J.; Dailey, J.; Yu, J.; Katz, H. E. Chemical and Biomolecule Sensing with Organic Field-Effect Transistors. *Chem. Rev.* **2019**, *119* (1), 3−35.
(5) Gumyusenge, A.; Tran, D. T.; Luo, X.; Pitch, G. M.; Zhao, Y.; Jenkins, K. A.; Dunn, T. J.; Ayzner, A. L.; Savoie, B. M.; Mei, J. Semiconducting Polymer Blends That Exhibit Stable Charge Transport at High Temperatures. *Science* **2018**, *362* (6419), 1131−1134.
(6) Inal, S.; Malliaras, G. G.; Rivnay, J. Benchmarking Organic Mixed Conductors for Transistors. *Nat. Commun.* **2017**, *8* (1), 1−7.
(7) Paulsen, B. D.; Tybrandt, K.; Stavrinidou, E.; Rivnay, J. Organic Mixed Ionic−Electronic Conductors. *Nat. Mater.* **2020**, *19* (1), 13−26.
(8) Tan, S. T. M.; Gumyusenge, A.; Quill, T. J.; LeCroy, G. S.; Bonacchini, G. E.; Denti, I.; Salleo, A. Mixed Ionic−Electronic Conduction, a Multifunctional Property in Organic Conductors. *Adv. Mater.* **2022**, *34* (21), 2110406−2110406.
(9) Ji, X.; Lin, X.; Rivnay, J. Organic Electrochemical Transistors as On-Site Signal Amplifiers for Electrochemical Aptamer-Based Sensing. *Nat. Commun.* **2023**, *14* (1), 1665.
(10) Harikesh, P. C.; Yang, C.-Y.; Wu, H.-Y.; Zhang, S.; Donahue, M. J.; Caravaca, A. S.; Huang, J.-D.; Olofsson, P. S.; Berggren, M.; Tu, D.; Fabiano, S. Ion-Tunable Antiambipolarity in Mixed Ion−Electron Conducting Polymers Enables Biorealistic Organic Electrochemical Neurons. *Nat. Mater.* **2023**, *22* (2), 242−248.
(11) Li, N.; Kang, S.; Liu, Z.; Wai, S.; Cheng, Z.; Dai, Y.; Solanki, A.; Li, S.; Li, Y.; Strzalka, J.; White, M. J. V.; Kim, Y. H.; Tian, B.; Hubbell, J. A.; Wang, S. Immune-Compatible Designs of Semiconducting Polymers for Bioelectronics with Suppressed Foreign-Body Response. *Nat. Mater.* **2025**, *25*, 124−132.
(12) Keene, S. T.; Lubrano, C.; Kazemzadeh, S.; Melianas, A.; Tuchman, Y.; Polino, G.; Scognamiglio, P.; Cinà, L.; Salleo, A.; van de Burgt, Y.; Santoro, F. A Biohybrid Synapse with Neurotransmitter-Mediated Plasticity. *Nat. Mater.* **2020**, *19* (9), 969−973.
(13) Roh, H.; Cunin, C.; Samal, S.; Gumyusenge, A. Towards Organic Electronics That Learn at the Body-Machine Interface: A Materials Journey. *MRS Commun.* **2022**, *12* (5), 565−577.
(14) Horowitz, G. Organic Field-Effect Transistors. *Adv. Mater.* **1998**, *10* (5), 365−377.
(15) Sirringhaus, H.; Brown, P. J.; Friend, R. H.; Nielsen, M. M.; Bechgaard, K.; Langeveld-Voss, B. M. W.; Spiering, A. J. H.; Janssen, R. a. J.; Meijer, E. W.; Herwig, P.; de Leeuw, D. M. Two-Dimensional Charge Transport in Self-Organized, High-Mobility Conjugated Polymers. *Nature* **1999**, *401* (6754), 685−688.
(16) Liu, C.; Huang, K.; Park, W.-T.; Li, M.; Yang, T.; Liu, X.; Liang, L.; Minari, T.; Noh, Y.-Y. A Unified Understanding of Charge Transport in Organic Semiconductors: The Importance of Attenuated Delocalization for the Carriers. *Mater. Horiz.* **2017**, *4* (4), 608−618.
(17) Coropceanu, V.; Cornil, J.; da Silva Filho, D. A.; Olivier, Y.; Silbey, R.; Brédas, J.-L. Charge Transport in Organic Semiconductors. *Chem. Rev.* **2007**, *107* (4), 926−952.
(18) Zhao, Y.; Zhao, X.; Roders, M.; Gumyusenge, A.; Ayzner, A. L.; Mei, J. Melt-Processing of Complementary Semiconducting Polymer Blends for High Performance Organic Transistors. *Adv. Mater.* **2017**, *29* (6), 1605056.
(19) Gumyusenge, A.; Zhao, X.; Zhao, Y.; Mei, J. Attaining Melt Processing of Complementary Semiconducting Polymer Blends at 130 °C via Side-Chain Engineering. *ACS Appl. Mater. Interfaces* **2018**, *10* (5), 4904−4909.
(20) Watson, J.; Castro, G. A Review of High-Temperature Electronics Technology and Applications. *J. Mater. Sci. Mater. Electron.* **2015**, *26* (12), 9226−9235.
(21) Goffri, S.; Müller, C.; Stingelin-Stutzmann, N.; Breiby, D. W.; Radano, C. P.; Andreasen, J. W.; Thompson, R.; Janssen, R. A. J.; Nielsen, M. M.; Smith, P.; Sirringhaus, H. Multicomponent Semiconducting Polymer Systems with Low Crystallization-Induced Percolation Threshold. *Nat. Mater.* **2006**, *5* (12), 950−956.
(22) Abe, M.; Mori, T.; Osaka, I.; Sugimoto, K.; Takimiya, K. Thermally, Operationally, and Environmentally Stable Organic Thin-Film Transistors Based on Bis[1]Benzothieno[2,3-d:2′,3′-D′]-Naphtho[2,3-b:6,7-B′]Dithiophene Derivatives: Effective Synthesis, Electronic Structures, and Structure−Property Relationship. *Chem. Mater.* **2015**, *27* (14), 5049−5057.
(23) Lee, E. K.; Lee, M. Y.; Park, C. H.; Lee, H. R.; Oh, J. H. Toward Environmentally Robust Organic Electronics: Approaches and Applications. *Adv. Mater.* **2017**, *29* (44), No. 1703638.
(24) Bagatella, S.; Roh, H.; Cavallaro, M.; Suriano, R.; Levi, M.; Gumyusenge, A. 3D-Printed Mixed Ionic-Electronic Conductive Polymer Composites for Long-Term Bioelectronic Sensing. *Adv. Mater. Technol.* **2025**, *10*, No. e01154.
(25) Gumyusenge, A.; Luo, X.; Ke, Z.; Tran, D. T.; Mei, J. Polyimide-Based High-Temperature Plastic Electronics. *ACS Mater. Lett.* **2019**, *1* (1), 154−157.
(26) Yang, G. G.; Kim, D.-H.; Samal, S.; Choi, J.; Roh, H.; Cunin, C. E.; Lee, H. M.; Kim, S. O.; Dincă, M.; Gumyusenge, A. Polymer-Based Thermally Stable Chemiresistive Sensor for Real-Time Monitoring of NO2 Gas Emission. *ACS Sens.* **2023**, *8* (10), 3687−3692.
(27) Zhang, S.; Hubis, E.; Girard, C.; Kumar, P.; DeFranco, J.; Cicoira, F. Water Stability and Orthogonal Patterning of Flexible Micro-Electrochemical Transistors on Plastic. *J. Mater. Chem. C* **2016**, *4* (7), 1382−1385.
(28) Zheng, Y. Q.; Liu, Y.; Zhong, D.; Nikzad, S.; Liu, S.; Yu, Z.; Liu, D.; Wu, H. C.; Zhu, C.; Li, J.; Tran, H.; Tok, J. B. H.; Bao, Z. Monolithic Optical Microlithography of High-Density Elastic Circuits. *Science* **2021**, *373* (6550), 88−94.
(29) Huang, W.; Chen, J.; Yao, Y.; Zheng, D.; Ji, X.; Feng, L.-W.; Moore, D.; Glavin, N. R.; Xie, M.; Chen, Y.; Pankow, R. M.; Surendran, A.; Wang, Z.; Xia, Y.; Bai, L.; Rivnay, J.; Ping, J.; Guo, X.; Cheng, Y.; Marks, T. J.; Facchetti, A. Vertical Organic Electrochemical Transistors for Complementary Circuits. *Nature* **2023**, *613* (7944), 496−502.
(30) Wu, C.; Li, C.; Yu, X.; Chen, L.; Gao, C.; Zhang, X.; Zhang, G.; Zhang, D. An Efficient Diazirine-Based Four-Armed Cross-Linker for Photo-Patterning of Polymeric Semiconductors. *Angew. Chem., Int. Ed.* **2021**, *60* (39), 21521−21528.
(31) Lai, Y.; Cheng, J.; Xie, M.; Chen, J.; Zhu, G.; Huang, W.; Feng, L.-W. Precisely Patterned Channels in a Vertical Organic Electrochemical Transistor with a Diazirine Photo-Crosslinker. *Angew. Chem., Int. Ed.* **2024**, *63* (18), No. e202401773.
(32) Lai, Y.; Sun, Y.; Tian, J.; Chen, J.; Huang, W.; Feng, L.-W. Separated Ionic-Electronic Conduction in Hydrophobic Conjugated Polymer/Hydrophilic Photocrosslinker Blends for Organic Electrochemical Transistors. *SmartMat* **2025**, *6* (2), No. e70011.
(33) Gao, L.; Zhang, Q.; Lai, Y.; Xie, M.; Liu, C.; Zhang, D.; Peng, Y.; Bai, L.; Wu, M.; Feng, L.-W.; Huang, W.; Yu, J.; Yu, X. High-Loading Homogeneous Crosslinking Enabled Ultra-Stable Vertical Organic Electrochemical Transistors for Implantable Neural Interfaces. *Nano Energy* **2024**, *129*, No. 110062.
(34) Gao, C.; Li, C.; Yang, Y.; Jiang, Z.; Xue, X.; Chenchai, K.; Liao, J.; Shangguan, Z.; Wu, C.; Zhang, X.; Jia, D.; Zhang, F.; Liu, G.; Zhang, G.; Zhang, D. Nonhalogenated Solvent Processable and High-Density Photopatternable Polymer Semiconductors Enabled by Incorporating Hydroxyl Groups in the Side Chains. *Adv. Mater.* **2024**, *36* (24), 2309256.
(35) Roh, H.; Yue, S.; Hu, H.; Chen, K.; Kulik, H. J.; Gumyusenge, A. Unraveling Polymer−Ion Interactions in Electrochromic Polymers for Their Implementation in Organic Electrochemical Synaptic Devices. *Adv. Funct. Mater.* **2023**, *33*, No. 2304893.
(36) Nhon, L.; Wilkins, R.; Reynolds, J. R.; Tomlinson, A. Guiding Synthetic Targets of Anodically Coloring Electrochromes through Density Functional Theory. *J. Chem. Phys.* **2021**, *154* (5), No. 054110.
(37) Savagian, L. R.; Österholm, A. M.; Ponder, J. F., Jr.; Barth, K. J.; Rivnay, J.; Reynolds, J. R. Balancing Charge Storage and Mobility in an Oligo(Ether) Functionalized Dioxythiophene Copolymer for

https://doi.org/10.1021/acsami.6c05214
ACS Appl. Mater. Interfaces XXXX, XXX, XXX−XXX

Organic- and Aqueous- Based Electrochemical Devices and Transistors. *Adv. Mater.* **2018**, *30* (50), 1804647−1804647.
(38) Kumar, A.; Welsh, D. M.; Morvant, M. C.; Piroux, F.; Abboud, K. A.; Reynolds, J. R. Conducting Poly(3,4-Alkylenedioxythiophene) Derivatives as Fast Electrochromics with High-Contrast Ratios. *Chem. Mater.* **1998**, *10* (3), 896−902.
(39) Ko, H. C.; Park, S.; Paik, W.; Lee, H. Electrochemistry and Electrochromism of the Polythiophene Derivative with Viologen Pendant. *Synth. Met.* **2002**, *132* (1), 15−20.
(40) Lee, B.; Seshadri, V.; Sotzing, G. A. Poly(Thieno[3,4-b]Thiophene)−Poly(Styrene Sulfonate): A Low Band Gap, Water Dispersible Conjugated Polymer. *Langmuir* **2005**, *21* (23), 10797−10802.
(41) Wu, C.-G.; Lu, M.-I.; Chang, S.-J.; Wei, C.-S. A Solution-Processable High-Coloration-Efficiency Low-Switching-Voltage Electrochromic Polymer Based on Polycyclopentadithiophene. *Adv. Funct. Mater.* **2007**, *17* (7), 1063−1070.
(42) Lepage, M. L.; Simhadri, C.; Liu, C.; Takaffoli, M.; Bi, L.; Crawford, B.; Milani, A. S.; Wulff, J. E. A Broadly Applicable Cross-Linker for Aliphatic Polymers Containing C−H Bonds. *Science* **2019**, *366* (6467), 875−878.
(43) Liu, K.; Rafique, S.; Musolino, S. F.; Cai, Z.; Liu, F.; Li, X.; Yuan, Y.; Bao, Q.; Yang, Y.; Chu, J.; Peng, X.; Nie, C.; Yuan, W.; Zhang, S.; Wang, J.; Pan, Y.; Zhang, H.; Cai, X.; Shi, Z.; Li, C.; Wang, H.; Deng, L.; Hu, T.; Wang, Y.; Wang, Y.; Chen, S.; Shi, L.; Ayala, P.; Wulff, J. E.; Yu, A.; Zhan, Y. Covalent Bonding Strategy to Enable Non-Volatile Organic Cation Perovskite for Highly Stable and Efficient Solar Cells. *Joule* **2023**, *7* (5), 1033−1050.
(44) Cuthbert, T. J.; Ennis, S.; Musolino, S. F.; Buckley, H. L.; Niikura, M.; Wulff, J. E.; Menon, C. Covalent Functionalization of Polypropylene Filters with Diazirine−Photosensitizer Conjugates Producing Visible Light Driven Virus Inactivating Materials. *Sci. Rep.* **2021**, *11* (1), 19029.
(45) Li, J.; Bi, L.; Musolino, S. F.; Wulff, J. E.; Sask, K. N. Functionalization of Polydimethylsiloxane with Diazirine-Based Linkers for Covalent Protein Immobilization. *ACS Appl. Mater. Interfaces* **2024**, *16* (1), 1−16.
(46) Simhadri, C.; Bi, L.; Lepage, M. L.; Takaffoli, M.; Pei, Z.; Musolino, S. F.; Milani, A. S.; DiLabio, G. A.; Wulff, J. E. Flexible Polyfluorinated Bis-Diazirines as Molecular Adhesives. *Chem. Sci.* **2021**, *12* (11), 4147−4153.
(47) Zhao, X.; Bi, L.; Khatir, B.; Serles, P.; Filleter, T.; Wulff, J. E.; Golovin, K. Crosslinking Inert Liquidlike Polydimethylsiloxane Brushes Using Bis-Diazirine Chemical Insertion for Enhanced Mechanical Durability. *Chem. Eng. J.* **2022**, *442*, No. 136017.
(48) Nazir, R.; Bi, L.; Musolino, S. F.; Margoto, O. H.; Çelebi, K.; Mobuchon, C.; Takaffoli, M.; Milani, A. S.; Falck, G.; Wulff, J. E. Polyamine−Diazirine Conjugates for Use as Primers in UHMWPE−Epoxy Composite Materials. *ACS Appl. Polym. Mater.* **2022**, *4* (3), 1728−1742.
(49) Kim, S.-M.; Kim, C.-H.; Kim, Y.; Kim, N.; Lee, W.-J.; Lee, E.-H.; Kim, D.; Park, S.; Lee, K.; Rivnay, J.; Yoon, M.-H. Influence of PEDOT:PSS Crystallinity and Composition on Electrochemical Transistor Performance and Long-Term Stability. *Nat. Commun.* **2018**, *9* (1), 3858.
(50) Kukhta, N. A.; Marks, A.; Luscombe, C. K. Molecular Design Strategies toward Improvement of Charge Injection and Ionic Conduction in Organic Mixed Ionic−Electronic Conductors for Organic Electrochemical Transistors. *Chem. Rev.* **2022**, *122* (4), 4325−4355.
(51) Osazuwa, P. O.; Lo, C.-Y.; Feng, X.; Nolin, A.; Dhong, C.; Kayser, L. V. Surface Functionalization with (3-Glycidyloxypropyl)-Trimethoxysilane (GOPS) as an Alternative to Blending for Enhancing the Aqueous Stability and Electronic Performance of PEDOT:PSS Thin Films. *ACS Appl. Mater. Interfaces* **2023**, *15* (47), 54711−54720.
(52) Musolino, S. F.; Mahbod, M.; Nazir, R.; Bi, L.; Graham, H. A.; Milani, A. S.; Wulff, J. E. Electronically Optimized Diazirine-Based Polymer Crosslinkers. *Polym. Chem.* **2022**, *13* (25), 3833−3839.
(53) Zhao, X.; Qiu, X.; Xue, H.; Liu, S.; Liang, D.; Yan, C.; Chen, W.; Wang, Y.; Zhou, G. Conjugated and Non-Conjugated Polymers Containing Two-Electron Redox Dihydrophenazines for Lithium-Organic Batteries. *Angew. Chem.* **2023**, *135* (9), No. e202216713.
(54) Das, I.; De, G. Zirconia Based Superhydrophobic Coatings on Cotton Fabrics Exhibiting Excellent Durability for Versatile Use. *Sci. Rep.* **2016**, *5* (1), 18503.
(55) Tan, S. T. M.; Lee, G.; Denti, I.; LeCroy, G.; Rozylowicz, K.; Marks, A.; Griggs, S.; McCulloch, I.; Giovannitti, A.; Salleo, A. Tuning Organic Electrochemical Transistor Threshold Voltage Using Chemically Doped Polymer Gates. *Adv. Mater.* **2022**, *34* (33), 2202359.
(56) De La Fuente Durán, A.; Liang, A. Y. L.; Denti, I.; Yu, H.; Pearce, D.; Marks, A.; Penn, E.; Treiber, J.; Weaver, K.; Turaski, L.; Maria, I. P.; Griggs, S.; Chen, X.; Salleo, A.; Chueh, W. C.; Nelson, J.; Giovannitti, A.; Mefford, J. T. Origins of Hydrogen Peroxide Selectivity during Oxygen Reduction on Organic Mixed Ionic−Electronic Conducting Polymers. *Energy Environ. Sci.* **2023**, *16* (11), 5409−5422.
(57) Song, Z.; Im, J.-H.; Ko, H.; Park, J.-H.; Lee, G.-Y.; Kang, M.-J.; Kim, M.-H.; Pyun, J.-C. Plasma Deposition of Parylene-C Film. *Mater. Today Commun.* **2021**, *26*, No. 101834.
(58) Ke, Z.; You, L.; Tran, D. T.; He, J.; Perera, K.; Gumyusenge, A.; Mei, J. Thermally Stable and Solvent-Resistant Conductive Polymer Composites with Cross-Linked Siloxane Network. *ACS Appl. Polym. Mater.* **2021**, *3* (3), 1537−1543.
(59) Li, X.; Perera, K.; He, J.; Gumyusenge, A.; Mei, J. Solution-Processable Electrochromic Materials and Devices: Roadblocks and Strategies towards Large-Scale Applications. *J. Mater. Chem. C* **2019**, *7* (41), 12761−12789.
(60) Rivnay, J.; Inal, S.; Collins, B. A.; Sessolo, M.; Stavrinidou, E.; Strakosas, X.; Tassone, C.; Delongchamp, D. M.; Malliaras, G. G. Structural Control of Mixed Ionic and Electronic Transport in Conducting Polymers. *Nat. Commun.* **2016**, *7* (1), 11287.
(61) Christiansen, D. T.; Ohtani, S.; Chujo, Y.; Tomlinson, A. L.; Reynolds, J. R. All Donor Electrochromic Polymers Tunable across the Visible Spectrum via Random Copolymerization. *Chem. Mater.* **2019**, *31* (17), 6841−6849.
(62) Cendra, C.; Giovannitti, A.; Savva, A.; Venkatraman, V.; McCulloch, I.; Salleo, A.; Inal, S.; Rivnay, J. Role of the Anion on the Transport and Structure of Organic Mixed Conductors. *Adv. Funct. Mater.* **2019**, *29* (5), 1807034.
(63) Kim, S. H.; Chung, S.; Kim, M.; Yoo, D.; Ok, E.; Kim, S.; Song, K. C.; Song, Y. J.; Kang, B.; Cho, K. Designing a Length-Modulated Azide Photocrosslinker to Improve the Stretchability of Semiconducting Polymers. *Adv. Funct. Mater.* **2023**, *33* (23), 2212127.
(64) Estrada, L. A.; Deininger, J. J.; Kamenov, G. D.; Reynolds, J. R. Direct (Hetero)Arylation Polymerization: An Effective Route to 3,4-Propylenedioxythiophene-Based Polymers with Low Residual Metal Content. *ACS Macro Lett.* **2013**, *2* (10), 869−873.

https://doi.org/10.1021/acsami.6c05214
ACS Appl. Mater. Interfaces XXXX, XXX, XXX−XXX